Defect governed zinc-rich columnar AZO thin film and contact interface for enhanced performance of thermocouple

Bingwei Luo[a], Lili Cao*[, b], Jinyang Zhang[b], Fei Luo[a], Haitao Zhou[a], Kexin Ma[a], Braulio Beltrán-Pitarch[c], Mauricio Solis-De la Fuente[c], Francisco Vidan Falomir[c], Jorge García-Cañadas*[, c]

[a]*Beijing Institute of Aeronautical Materials, Aero Engine Corporation of China, Beijing 100095, China*

[b]*Key Laboratory of the Ministry of Education for Optoelectronic Measurement Technology and Instrument, Beijing Information Science & Technology University, Beijing, 100192, China*

[c]*Department of Industrial Systems Engineering and Design, Universitat Jaume I, Campus Del Riu Sec, 12006, Castelló de la Plana, Spain*

*Corresponding author.

E-mail address: lilicao@bistu.edu.cn; garciaj@uji.es

Abstract

The research on the stable thermoelectric properties and contact interface of high-precision thin-film thermocouple legs far behind the demand. In this study, a zinc-rich Al-doped ZnO (AZO) thin film was fabricated, in which the carriers were mainly donated by the Al dopant, and the oxygen defects migrated together, forming cage defects. Then, an indium tin oxide (ITO)/AZO thin-film thermocouple was prepared. It had a special temperature-dependent voltage curve due to the effects of cage defects on the thermoelectric properties of the AZO thin film and interfacial electron diffusion. When the zinc atoms in the cage defects were excited after

annealing, a linear relationship between the temperature and voltage was obtained. The Seebeck coefficient of the thermocouple was constant at 168 μV K^{-1} over the entire measured temperature range. In addition, the calculated error of the thermocouple was lower than 1% from 50 °C to 500 °C, showing good repeatability. These results showed that defect engineering could effectively be used to improve the temperature range stability of thermoelectric materials and optimize the precision of thin-film thermocouples.

Keywords: AZO; ITO; thin film; thermocouple; thermoelectric; mechanism

1. Introduction

Thermoelectric effects, including the Seebeck, Pertier, and Thomson effects, have attracted increasing attention because of their potential applications in low-grade heating and cooling, and are expected to play significant roles in energy conversion. [1–3] Thermocouples represent the most significant application of the Seebeck effect, and require high stability and precision in the temperature detection range. [4–6] Recently, thin-film thermocouples have been shown to have significant advantages, including a real-time data recording ability, quick response, high accuracy, and low impact on the base components. [7–10] As alternatives to noble metal thermocouples, conductive oxides have gained attention because of their large Seebeck coefficients, excellent chemical and phase stabilities, high melting points, and resistance to oxidation at elevated temperatures. [11–13]

Al-doped ZnO (AZO), an n-type semiconductor with good electrical properties,

optical transmittance, and gas absorption, has been studied in numerous fields such as thin-film transistors, gas sensors, solar cells, and thermoelectric devices. [14–19] In one study, the Seebeck coefficient of AZO reached -560 μV K^{-1}, with a low electrical conductivity of 40–300 S m^{-1}. [20] Although a high Seebeck coefficient can effectively improve the sensitivity, a long application distance for a thermocouple reduces the resistivity. Moreover, a wide temperature range stability for the Seebeck coefficient is required for a simplified calculation between the temperature and voltage. Both the Seebeck coefficient and resistivity of AZO materials are governed by a temperature-dependent electronic transport mechanism, which has not yet been fully understood. In AZO materials, the concentration of oxygen vacancies plays a significant role in high-temperature electronic transport. This is because oxygen vacancies are unstable when applied in an oxygen atmosphere at high temperatures. [21–23] Electronic transport mechanisms such as grain boundary scattering and defect engineering have been successfully applied to the synthetic control of the resistivity and Seebeck coefficient of a thermoelectric material. [24, 25] Thus, the use of defect engineering to control the generation and transport of carriers is critical when an AZO thin film is applied as one arm of a thermocouple.

In contrast to a traditional metal-based thermocouple with a directly welded interface, the contact barrier impedes electronic transport through the interface, and the contact interfacial voltage will have an effect on the entire voltage of the thermocouple when two different n-type semiconductor materials are in direct contact. Semiconductor junctions have been studied and applied to the performance

control of solar cells. [26, 27] It is important to further improve the performance of oxide thin-film thermocouples by investigating the mechanism and evolution of the contact interface. However, few researchers have focused on the effect of the interface junction on the overall performance of a thermocouple.

In this study, zinc-rich columnar AZO thin films were fabricated using magnetron sputtering. The thermoelectric performance of the AZO thin film was controlled by the design of cage defects. Subsequently, a thermocouple was formed using an amorphous ITO thin film and columnar AZO thin film. The interface structure and interfacial electronic transport mechanisms were also investigated. Controlled by the special defect structure of cage defects, the variation in the thin-film thermocouple was strongly reduced when tested up to 500 °C, obtaining highly repeatable curves.

2. Experimental Section

2.1 Preparation of ITO and AZO thin films for characteristic measurement

The ITO and AZO thin films were prepared using a magnetron sputtering deposition system. ITO (In_2O_3/SnO_2 90/10 wt%) and AZO (ZnO/Al_2O_3 98/2 wt%) targets (Beijing General Research Institute for Nonferrous Metals) with purities of 99.99% were used. They each had a diameter and thickness of 76.2 mm and 4 mm, respectively. The target material was cleaned by pre-sputtering for 10 min before each deposition. Quartz glass (10 mm × 10 mm × 1 mm) and alumina (5 mm × 15 mm × 1 mm) substrates were employed to obtain different measurements. They were cleaned by sonication, immersed in alcohol and deionized water for 15 min, and then dried in

an air atmosphere. The deposition was carried out at temperature of 200 ℃, where the distance from the target to the substrate was 90 mm. A sputtering power level of 60–80 W was maintained for 90–120 min. the base pressure of the deposition chamber was set to a value of less than 3.0×10^{-4} Pa, and the working gas pressure was controlled in a 0.4 Pa range by flowing 25 sccm of Ar as the sputtering gas. The annealing process was maintained for 3 h in air at 500 °C to investigate the high-temperature properties.

2.2 Preparation of Pt/ITO/AZO/Pt thin film thermocouple

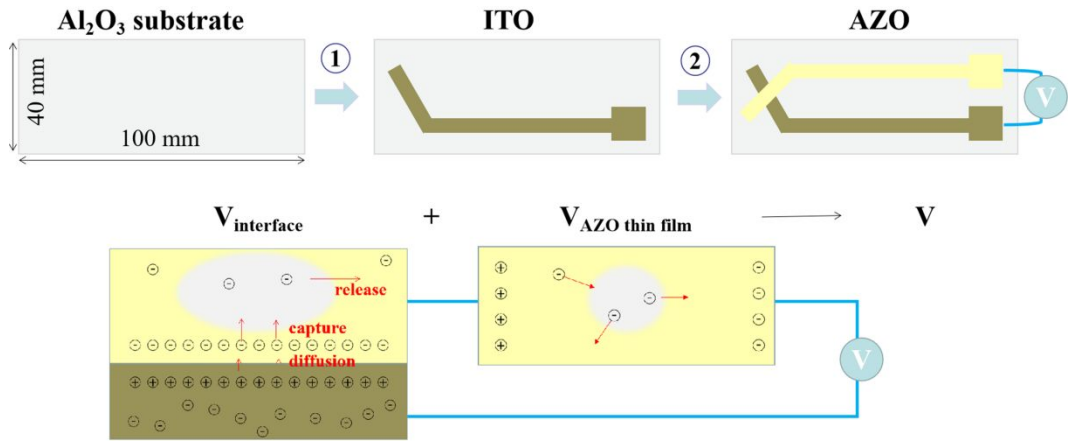

Figure 1 Fabrication process and mechanism for ITO/AZO thin-film thermocouple. The thermocouple was fabricated by a two-step deposition (ITO thin film and AZO thin film), and the whole output voltage was contributed by connect interface and thin films.

As shown in Figure 1, a thin-film thermocouple was prepared on an Al_2O_3 substrate (10 cm × 4 cm × 1 mm). It was formed using ITO and AZO thin films with one contact interface and Pt films as electrodes. The widths of the ITO and AZO

thermoelectric legs were 5 mm. All the films were deposited using magnetron sputtering (ShenYang Pengcheng Vacuum Technology Co., Ltd, CK450D). The ITO thermoelectric arm was deposited at 200 ℃, 0.4 Pa, and 77 W, whereas the AZO thermoelectric arm was deposited at the same temperature and pressure but with a different sputtering power of 70 W. The samples were annealed at 500 °C for 3 h in a furnace (Nabertherm 400-1) with a heating rate of 3 °C/min. For the electrodes, a thin chromium layer (~5 nm) was first deposited by sputtering (Quorum Technologies, Q300 TD plus), followed by Pt film deposition at a rate of 25 nm/min for 1 min.

2.3 Films characterizations and thermocouple measurements

The morphologies of the ITO and AZO thin films were characterized using scanning electron microscopy (SEM; JEOL SU 8010) and transmission electron microscopy (TEM) equipped with energy dispersive spectroscopy (EDS) (FEI Talos F200X). Before the TEM measurements, the sample was prepared using a focused ion beam (FIB; FEI G4 UC). The structure of the films was analyzed using X-ray diffraction in a 2θ range of 10° to 90° with Cu Kα radiation (Bruker D8 Advance diffractometer). The thermoelectric properties (resistivity and Seebeck coefficient) were measured using a four-probe system (Cryoall CTA-3S). The optical properties were tested using a UV-Vis-NIR spectrophotometer (Hitachi, UH4150).

The performance of the thermocouple was evaluated by measuring the open-circuit voltage of the device, using a Keithley 2601 source meter in the four-probe mode, at different hot-side temperatures, from room temperature up to 550 °C, while keeping

the cold side temperature constant at 25 ± 1 °C. A copper block (40 mm × 40 mm × 20 mm) with four inserted cartridge heaters (Watlow, ref. E1J49-L1) was used as the heat source, and a copper block with embedded water circulation was used as the heat sink. The temperature of the circulating water was controlled using a PolyScience (SD07R-20-A12E) circulation bath. Thermal grease (RS; ref. 2173835) was used as the thermal interface material to improve the thermocouple/copper block thermal contact on the cold side. Two K-type thermocouples (RS, ref. 814-0134) were employed to monitor the hot- and cold-side temperatures of the thin-film thermocouple. They were attached to the substrate at positions close to the hot-side junction and Pt electrodes with a small amount of thermal grease at their tips. A variable transformer (RS; ref. 890-2878) was used to power the heaters and achieve different hot-side temperatures. All the measurements were performed in a closed stainless steel chamber.

3. Results and discussion

3.1 Structure of zinc-rich columnar AZO thin film

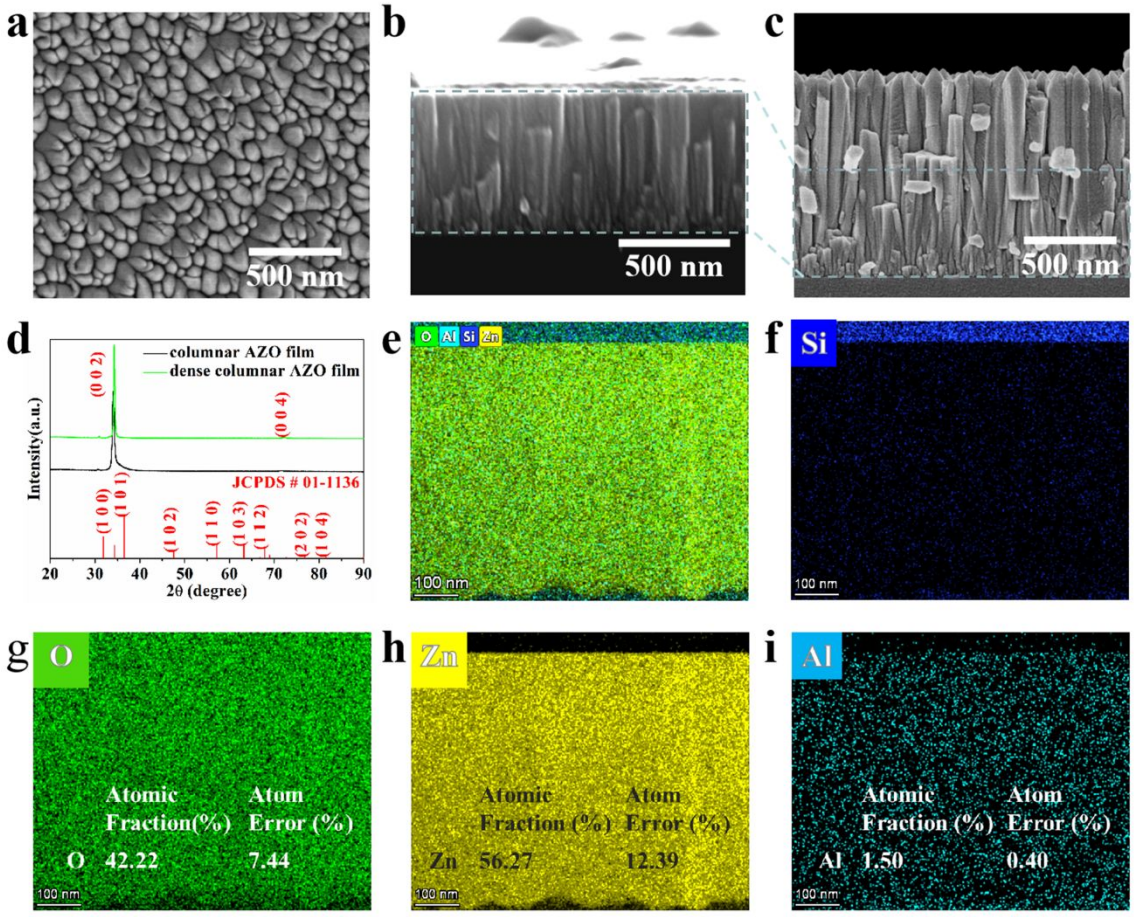

Figure 2 SEM images of AZO columnar thin films: (a) surface, and cross-sectional view of (b) dense columnar thin film (550 nm) fabricated using 90 min deposition process and (c) columnar AZO film (1 μm) fabricated using 120 min deposition process; (d) XRD patterns of AZO columnar thin films with different thickness; and EDS images of dense columnar AZO thin film: (e) the entire distribution of four kinds elements, and (f-i) the distributions of Si, O, Zn and Al, respectively.

Columnar AZO thin films with two thicknesses were obtained by magnetron sputtering with different deposition times. Figures 2(a–c) show SEM images of the AZO columnar thin film. It can be observed that the particles were uniformly distributed, as shown in the top view SEM images of Figure 2(a). The thickness of the AZO thin film fabricated using a 90 min deposition process was approximately 550 nm, while it was 1.08 μm when using the 120 min deposition process, as shown in the cross-sectional view images. It should be noted that the growth rate in the last 30 min

was three times that in the first 90 min. This was attributed to the change in the particle size during the growing process. Initially, the dense columnar thin film was composed of small particles, and large particles were formed via separated crystal epitaxial growth. Thus, the diameter of a single column gradually increased from the bottom to the top, showing good crystallization and a uniform shape. Figure 2(d) shows the XRD patterns of the AZO columnar thin films prepared using different sputtering times, which are in accordance with the standard XRD pattern of ZnO. The XRD diffractograms corroborated the preferential orientation of the columnar thin film, indicating that the AZO films grew optimally along the direction of the (002) crystal plane. The high intensity of the (002) crystal plane demonstrated the good crystallinity and high orientation of the AZO thin films with different thicknesses, which was consistent with the SEM results.

Figures 2(e–i) show the EDS energy spectrum of the AZO film tested using the TEM equipment. Four elements, Si, O, Zn, and Al, were detected. The entire image consisted of two parts, with an obvious boundary between the top and bottom. Elemental Si was distributed in the top part, and Zn and Al were uniformly distributed in the bottom part, indicating that the top layer was a quartz glass substrate, and the bottom layer contained the AZO thin film. The atomic fractions of O, Zn, and Al were 42.22, 56.27, and 1.50, respectively. The atomic fraction of Zn was 14.05% higher than that of O, indicating that the thin film was a zinc-rich material. However, no impurity phase was observed in the SEM images and XRD patterns, suggesting that the zinc-rich thin film was a structure- or defect-induced material, rather than a

compound of Zn and ZnO. In addition, Al was lightly doped into the ZnO thin film, with a Zn-to-Al atomic ratio of 37.5, which was higher than the ratio of the target before sputtering and assisted in increasing the carrier concentration.

The microstructure of the zinc-rich AZO thin films was investigated using TEM measurements. The atomic structures and morphologies of the AZO thin films are shown in Figure 3. Based on the cross-sectional view (Figure 3(a)), the thickness of the AZO column increased from approximately 30 nm to 70 nm, and the columns were densely connected without obvious gaps and cracks. Fewer large-scale defects were produced along the growth direction. Thus, the AZO thin film exhibited good crystallinity, which was consistent with the SEM images and XRD patterns. This demonstrated that the zinc-rich thin film was not composed of Zn and ZnO particles, but was a single-phase crystal. Two areas were selected to study the crystal interfaces and nanocrystals. Figure 3(b) shows the interface between the AZO thin film and the substrate without cracks, indicating strong bonding. The distinct morphologies of the nanoparticles (~5 nm) could be ascribed to epitaxial growth along the glass substrate, which led to a high bonding strength. High-resolution transmission electron microscopy (HRTEM) (Figure 3(c)) showed clear nano-boundaries between two neighboring particles. Although the lattice fringes of the AZO nanocrystals appeared to be arranged regularly, they were not long-range ordered structures with a small dislocation between two units, including two or three atoms. As the inset selected area electron diffraction (SAED) pattern shows, the facular points were connected, forming a circle demonstrating the low crystallinity of the AZO thin film neighboring

the substrate.

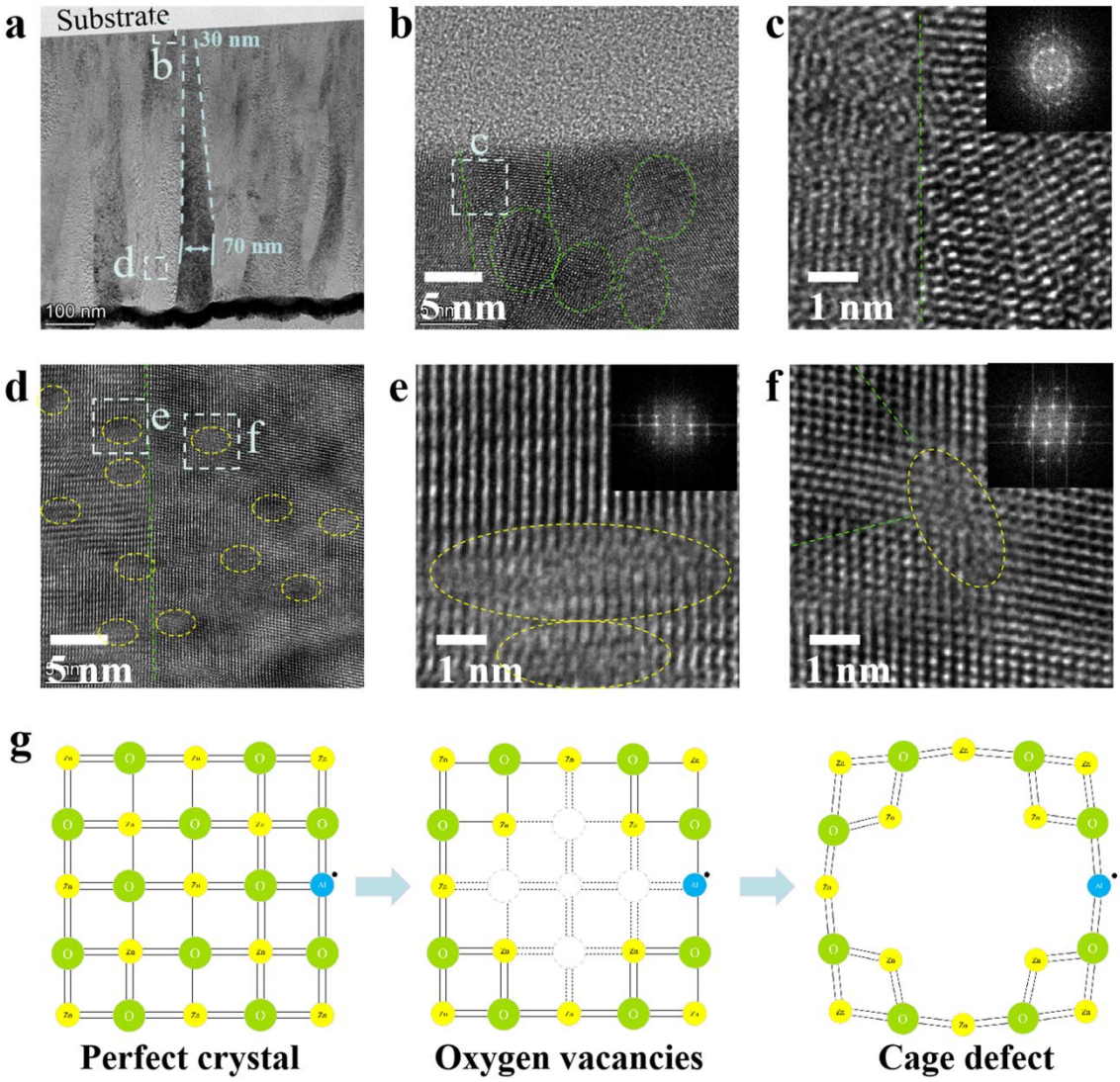

Figure 3 (a) TEM image of dense columnar AZO thin film; (b) HRTEM image of AZO thin film neighboring substrate, and (c) the magnified image and related inset SAED pattern; (d) HRTEM image of two neighboring AZO columns, and (e, f) the magnified images and related inset SAED patterns of both sides of the connect interface; (g) schematic diagram of defect formation.

Compared to the low crystallinity of the AZO thin film neighboring the substrate, the film in the upper area had high crystallinity, accompanied by high-density defects, as shown in Figure 3(d). The atoms were not restricted by the boundary between the two columns, leading to the formation of a consecutive crystal structure disrupted by a long-range dislocation. High-density defects were uniformly distributed in the

columnar thin films, which may have been the main reason for the zinc-rich structure. The HRTEM images (Figures 3(e) and (f)) show the high crystallinity and different lattice fringe structures between two neighboring columns, which could be verified by the striking mottled patterns shown in the inset SAED patterns. Furthermore, the size of the defects was approximately 3–7 nm. These were formed by atom diffusion and point defect aggregation, and they were mainly oxygen vacancy defects. A large number of oxygen vacancies led to the destruction of the crystal structure of the AZO thin film, and a new structure was formed to migrate to a stable state. Figure 3(g) presents a schematic diagram of the defect formation using a representative planar grid structure containing O, Zn, and Al. When defects gathered in one area, one Zn atom and four O atoms were lost, forming a cage defect. The internal surface of this cage was filled with Zn with a dangling bond, resulting in a stable and electroneutral space. This phenomenon is often observed on material surfaces. Moreover, oxygen defects led to lattice distortion. Thus, the continuous lattice structure was broken up, and new crystal boundaries were formed. These results also demonstrated that the zinc-rich phenomenon was caused by defects.

3.2 Thermoelectric properties of ITO/AZO columnar thin films

High-temperature thermocouples are a significant application of conductive ceramics and have attracted increasing attention. A zinc-rich AZO thin film was used to fabricate one of the two arms of a thermocouple. Thermocouples operate based on the Seebeck effect, where the difference in the Seebeck coefficients of the two arms plays a critical role in the output voltage. Hence, an ITO thin film was chosen as the

other arm of the thermocouple because of its low resistivity and Seebeck coefficient. An ITO thermoelectric arm composed of small particles was deposited on the substrate to guarantee good interface contact with the bottom crystal structure of the AZO thin film. The fabrication process for the ITO/AZO thin-film thermocouple is illustrated in Figure 1. In the first step, the ITO thin film was deposited on a clean Al_2O_3 substrate. The structure of the ITO film was analyzed using XRD, as shown in Figure 4(a). One characteristic peak was observed at 30.59°, which was correlated with the peak of the glass substrate and (222) crystalline plane according to the In_2O_3 standard pattern. The low-intensity diffraction peak and broad width of the peak showed that the ITO columnar thin film had a lower crystallinity and smaller particle size, which led to a high bonding strength with the AZO thin film. The cross-sectional SEM images show that the ITO thin film had a dense structure, with a thickness of 1.00 μm, which was close to that of the AZO thin film. The atomic In/Sn ratio obtained from the EDS spectrum was 12.6, revealing that the In_2O_3 was heavily doped with Sn. It can be seen that the ITO thin film was composed of arranged columns on the upper part and a dense planar part. These arranged columns were a result of a vertical crack during the fracture process, which acted like glass. In the second step, the AZO thin film was deposited on the substrate and ITO thin film to obtain the second arm of the thermocouple and contact interface as the temperature test position.

The output voltage of the thermocouple was dependent on the Seebeck coefficients. Therefore, the temperature-dependent Seebeck coefficients and resistivities of the AZO and ITO thin films were measured using a four-probe system. As shown in

Figures 4(c) and (d), the Seebeck coefficients of the ITO and AZO thin films were negative, indicating n-type semiconductors. Compared with the AZO thin film, the ITO thin film exhibited a stable Seebeck coefficient and resistivity with increasing temperature, whereas the AZO thin film exhibited special temperature-dependent characteristics. The absolute Seebeck coefficient of the AZO thin film increased from 23 $\mu V\ K^{-1}$ to 125 $\mu V\ K^{-1}$ with increasing temperature until 400 °C, after which it decreased from 125 $\mu V\ K^{-1}$ to 100 $\mu V\ K^{-1}$ in the temperature range of 400–550 °C. The resistivity of the AZO thin film exhibited a different trend. The highest resistivity of 470 $\mu\Omega$ m was achieved at 250 °C, with an increase in the resistivity before 250 °C and a decrease in the resistivity after 250 °C. The high resistivity and low Seebeck coefficient were affected by the defect structure, which leads to low weighted mobility, transport coefficient and effective mass (calculated based on the equations in Reference 28), respectively.

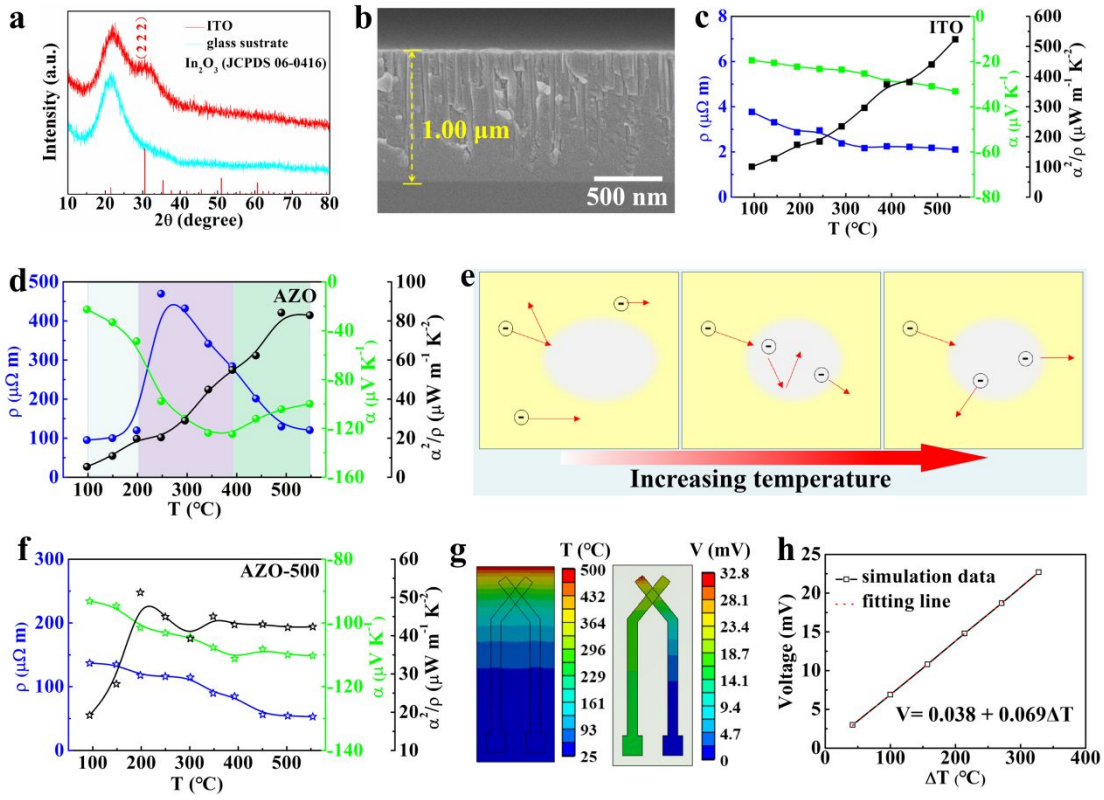

Figure 4 (a) XRD patterns of ITO thin film and glass substrate; (b) cross-sectional SEM image of ITO thin film; (c, d, f) thermoelectric properties (resistivity, Seebeck coefficient and power factor) of ITO thin film, AZO thin film before and after being annealed at 500 °C, respectively; (e) electronic transport mechanism of AZO thin film; (g) simulation results of temperature and voltage distribution of thin-film thermocouple; (h) relationship between voltage and temperature differences calculated by finite element analysis.

To accurately understand the mechanism of the electronic transport properties, Figure 4(e) shows the electronic transport mechanism of the AZO thin films with cage defects. The special temperature-dependent Seebeck coefficient and resistivity were mainly attributed to the special structure, as follows.

(1) The high resistivity of the AZO thin film was attributed to the low carrier concentration (-9.02 × 10^{19} cm^{-3}), mobility (5.1 cm^2 V^{-1} s^{-1}), and weighted mobility (3.0 cm^2 V^{-1} s^{-1}), as listed in Table 1. The carrier concentration was generated by the Al dopants and oxygen vacancies. The cage defects led to a reduced number of

separate oxygen vacancies, and electrons were mainly provided by the lightly doped Al element, which helped improve the stability of the AZO thin film. Thus, the carrier concentration of the AZO thin film was lower than that of the ITO thin films with a large number of oxygen vacancies and large amount of Sn dopant. As shown in Figure 3, there were many cage defects and crystal interfaces in the AZO thin film, which aggravated electron scattering, causing the low carrier mobility.

(2) As discussed above, the internal surface of the cage defect was filled with Zn with a dangling bond, forming a zinc-rich thin film, which was excited with an increase in temperature. The exited Zn in the cage defects could capture electrons and establish a more stable structure, leading to an approximately 50% reduction in the carrier concentration (-4.49×10^{19} cm^{-3}) and increased resistivity, along with a stable chemical component. With increasing temperature, an increasing number of Zn atoms in the cage defects were excited, along with a decrease in the carrier concentration. With a further increase in temperature, the captured electrons were released, attaining a dynamic capture and release equilibrium. The absolute value of the Seebeck coefficient increased with the temperature, as shown in Figure 4(a), which was inversely proportional to the carrier concentration based on the thermoelectric theory. Thus, the voltage of the thermocouple was enhanced after annealing. On the other hand, the crystal interfaces caused by crystal distortion were modified by atom diffusion at high temperatures, leading to a higher mobility (12.5 cm^2 V^{-1} s^{-1}) and reduced resistivity.

Owing to the cage defects and modified carrier mobility, the Seebeck coefficient

(-93−-110 μV K^{-1}) and resistivity (136−53 μΩ m) of the AZO thin films were stable after being annealed at 500 °C, consistent with the changes of effective masses and transport coefficients as shown in Table 1. Although the resistivity was higher than the value of bulk material reported in reference 20, the Seebeck coefficient are in agreement with the related results. [20, 29, 30] The power factor also increased with the highest value of 43 μW m^{-1} K^{-2}, which is in agreement with previous results in the Al-doped ZnO. [20, 30] The electronic properties indicated that the special capture-release process helped to enhance the electrical properties of the thermocouples.

Table 1 Transport properties of AZO and ITO thin films: n_H, μ_H, μ_w, m*, m_e and σ_{E0} are Hall carrier concentration, Hall carrier mobility, weighted mobility, effective mass, mass of electron, and transport coefficient, respectively.

Sample	n_H (cm^{-3})	μ_H (cm^2 V^{-1} s^{-1})	μ_w (cm^2 V^{-1} s^{-1})	m^*/m_e	σ_{E0} ($\times 10^4$ S m^{-1})
AZO	-9.02×10^{19}	5.1	3.0	0.70	0.09
AZO-200 °C	-8.20×10^{19}	5.6	-	-	-
AZO-500 °C	-4.49×10^{19}	12.5	7.8	0.72	0.24
ITO	-7.55×10^{20}	27.4	72.1	1.91	2.18
ITO-500 °C	-7.32×10^{20}	26.0	-	-	-

Table 2 Parameters of thin films and substrate: Seebeck coefficient, resistivity and thermal conductivity.

Sample	Seebeck coefficient ($\mu V\ K^{-1}$)	Resistivity ($\mu\Omega$ m)	Thermal conductivity ($W\ m^{-1}\ K^{-1}$)
AZO thin film	-100	100	20
ITO thin film	-20	2	20
Substrate	-	-	10

The temperature-dependent Seebeck coefficient had a significant effect on the output voltage of the thermocouple. Figures 4(g) and (h) show the simulated temperature and voltage distributions of the ITO/AZO thin-film thermocouple, respectively. Different temperatures of 100 °C, 200 °C, 300 °C, 400 °C, 500 °C, and 600 °C were applied to one side of the thermocouple, while the ambient temperature was fixed at 25 °C, and the air convection coefficient was set to 5 $W\ K^{-1}\ m^{-2}$. The properties of the thin films and substrates are presented in Table 2. As shown in Figure 4(g), the temperature was distributed in half the area of the substrate near the hot side. The voltage was generated by the electronic transport of the AZO thin film, whereas the voltage of the ITO thin film was uniform from the hot side to the cold side because of the low Seebeck coefficient and high thermal conductivity. The ITO thin film acted as an electrode in the thin-film thermocouple. In addition, the output voltage increased linearly with an increase in the temperature difference, with a Seebeck coefficient of 69 $\mu V\ K^{-1}$.

3.3 Interfacial electronic transport mechanism

The thin-film thermocouples consisted of three parts: the ITO thin film arm, AZO thin film arm, and interface connecting them. The electrical properties of the

thermocouple were dependent not only on the Seebeck coefficients of the thin films, but also on the contact interface. Figure 5(a) shows the morphology of the interface between the ITO and AZO thin films. It can be seen that the AZO thin film was closely linked with the ITO thin film, with an obvious interface line. The thickness of the ITO thin film was approximately 1.01 μm, indicating that the deposition of the AZO thin film had little effect on the ITO thin film. However, the AZO thin film (740 nm) on the ITO thin film was thinner than the AZO thin film deposited on the substrate. Notably, the AZO thin film deposited on the ITO had a morphology similar to that of the dense columnar AZO thin film shown in Figure 1(b), demonstrating the lower growth rate of the AZO thin film on the ITO. The element diffusion spectrum measured by EDS indicated that the diffusion between the AZO thin film and ITO thin film was controlled, which had a significant effect on the electronic transport across the interface.

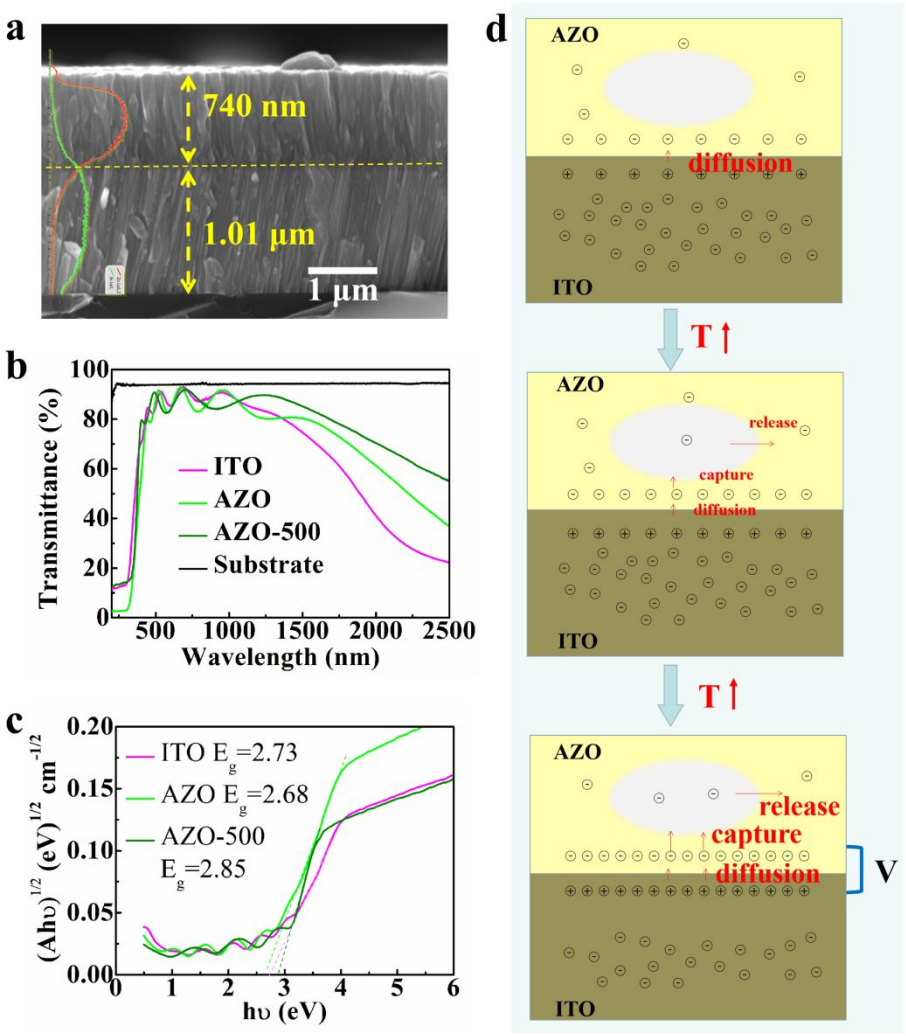

Figure 5 (a) SEM image of contact interface with an inset element distribution profile (the red and green lines); (b) UV-VIS-NIR spectra of ITO and AZO thin films; (c) band gap of ITO and AZO thin films calculated from the UV-VIS-NIR spectra and (d) interfacial electronic transport mechanism.

To study the interfacial properties and mechanism, the UV-VIS-NIR spectra were obtained to calculate the band gaps of the ITO and AZO thin films. Table 1 lists the carrier concentrations of the thin films before and after annealing, which played a significant role in the bandgap. As shown, the value of the ITO thin films remained stable, changing little before and after the annealing process, because the AZO thin film had only half the carrier concentration after being annealed at 500 °C in air. Hence, the UV-VIS-NIR spectra of the AZO thin film before and after being annealed

at 500 °C and the ITO thin films were detected.

As Figure 5(b) shows, the transmittance values of all the thin films were above 80% in the visible wavelength range, In contrast, the transmittance was inversely proportional to the carrier concentration (-7.55×10^{20} cm^{-3}, -9.02×10^{19} cm^{-3}, -4.49×10^{19} cm^{-3} for the ITO thin film, AZO thin film, and AZO thin film after being annealed at 500 °C, respectively) in the near-infrared wavelength range because of the absorption and reflection of carriers in this range. The band gap values were calculated based on the transmittance spectrum, and are shown in Figure 5(c). The band gap of the ITO thin film was 2.73 eV, which was between the values for the AZO thin films before and after annealing (2.68 eV and 2.85 eV). Similar values implied that there was no or only a small barrier formed when the ITO and AZO thin films were connected together. Therefore, electrons could be smoothly transported through the interface, and the output voltage generated at the interface depended on the difference in the carrier concentrations, which helped to form a linear relationship between the voltage and temperature difference. A schematic of the interfacial electronic transport mechanism is shown in Figure 5(d).

Based on the above results, it was concluded that the electrical properties of the ITO/AZO thin-film thermocouple depended on the Seebeck coefficient of the AZO thin film and the contact interface, both of which were affected by the defect structure of the AZO thin film. The AZO thin film had a band gap similar to that of the ITO thin film; therefore, the electrons could diffuse from one thin film to the other, through a very small barrier. There were two steps for the electronic transport through

the interface. In the first step, when the two kinds of thin films were connected to each other, the difference in the carrier concentrations drove electrons through the interface from the ITO thin film to the AZO thin film, achieving a balanced carrier concentration. With increasing temperature, an increasing number of electrons crossed the contact interface, and a built-in voltage formed, which satisfied the equilibrium condition of the carrier concentration at the contact interface for both holes and electrons. In the second step, zinc atoms in the cage defects were excited at higher temperatures, and electrons were captured by the cage defects, resulting in a new balance and higher voltage.

An annealing process was performed to excite the zinc atoms in the cage defects and decrease the carrier concentration as the electrons were captured by the cage defects. In addition, the difference in the carrier concentrations between the AZO and ITO thin films was higher, leading to a higher built-in voltage. Because the zinc atoms were excited during the annealing process, the sharp increase in the voltage with increasing temperature disappeared. Therefore, the built-in voltage depended on the difference in the carrier concentrations, which stabilized the interface Seebeck coefficient. However, a similar band gap reduced the electronic transition caused by the interface barrier, which was also the reason for the linear increase in voltage with increasing temperature. In summary, the built-in voltage at the contact interface, which depended on the special defect structure of the AZO thin film, was the main contributor to the output voltage of the thermocouple.

3.4 Electrical properties of thermocouple

Figure 6 shows the voltage readings of the ITO/AZO thin-film thermocouple as a function of the temperature difference (ΔT). As Figures 6(a) and (b) show, there were three parts to the testing. (1) Based on electron diffusion at the interface and scattering in the thin films, the output voltage linearly increased with ΔT. When ΔT increased to 280 °C, the voltage sharply increased. In the second and third tests, the temperature difference was limited to a temperature difference range of 0–250 °C, and the output voltage values were enhanced compared with those in the first test, but the two test curves almost overlapped. The above results demonstrated that the output voltage values were stable for a temperature difference below 250 °C after the annealing process. (2) When zinc atoms in the cage defects were excited in the fourth test, the output voltage curve showed an increasing trend similar to those seen in the second and third tests below 250 °C. When the hot end of the thermocouple was subjected to further heating, the output voltage showed a sharp increase at a temperature difference of 350 °C and reached the highest value when the temperature reached 500 °C, which indicated that the electronic transport mechanism could have changed. (3) After annealing, the Zn atoms in the cage defects were completely excited. Thus, in the fifth test, the output voltage increased with the temperature difference until 530 °C, with triple the value obtained in the first test. The special curves at different temperatures suggested that the ITO/AZO thin-film thermocouple exhibited different performances after being annealed at different temperatures (300 °C and 500 °C).

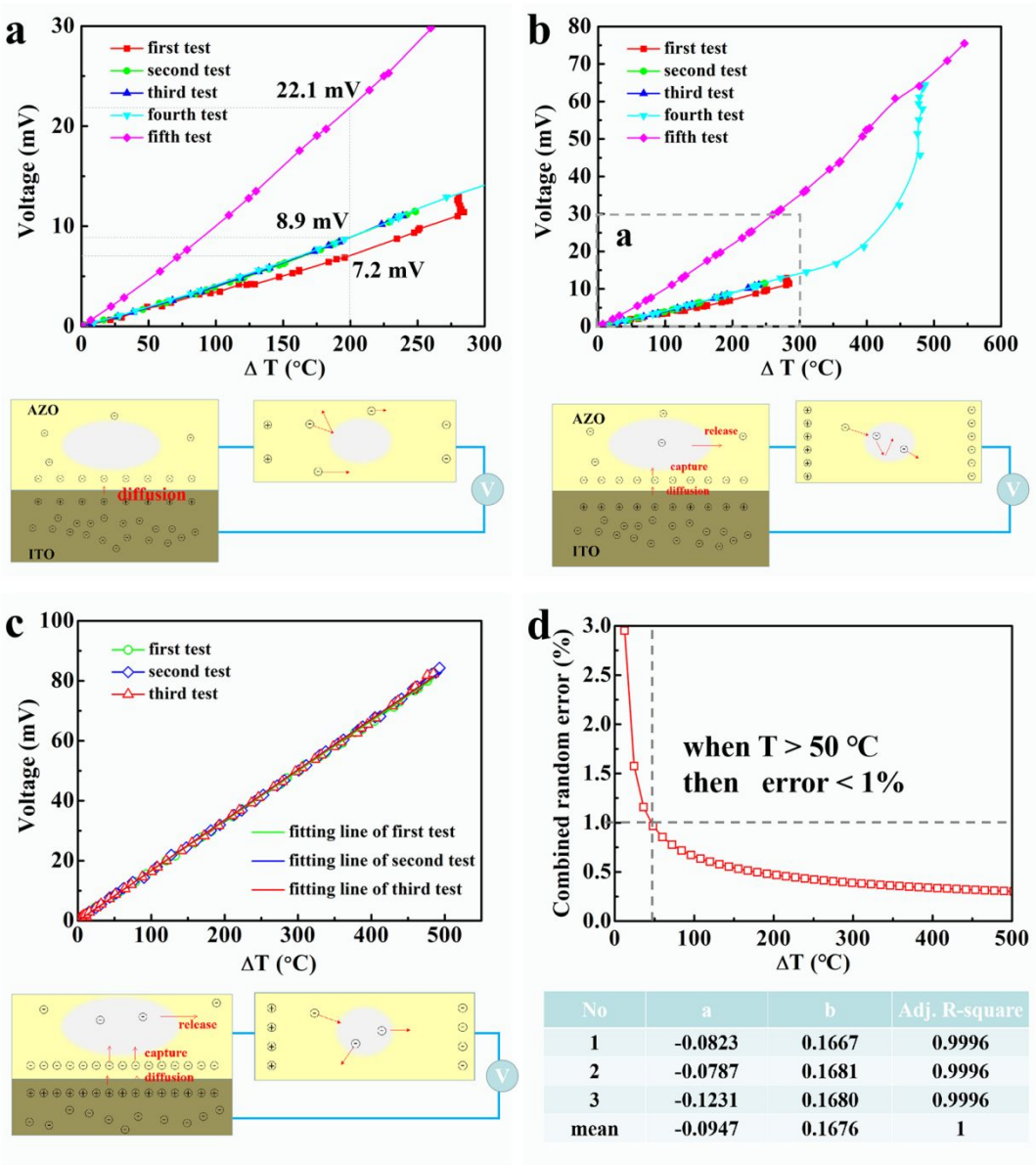

No	a	b	Adj. R-square
1	-0.0823	0.1667	0.9996
2	-0.0787	0.1681	0.9996
3	-0.1231	0.1680	0.9996
mean	-0.0947	0.1676	1

Figure 6 Measured voltage of the thin-film thermocouple with different values of temperature differences between hot side and cold side before and after annealing with the related transport mechanism below the diagrams: (a) temperature difference in range from 0 to 300 °C before annealing process; (b) in range from 0 to 500 °C before annealing process; (c) in range from 0 to 500 °C after annealing process; and (d) combined random errors and the fitting parameters of three tests after annealing process.

As shown by the above results, the optimal values were obtained after annealing at 500 °C (fourth test). Thus, the thin-film thermocouple was annealed at 500 °C in air, and the electrical properties were tested. Figure 6(c) shows the voltage reading of the thin-film thermocouple as a function of the temperature difference for the three

different experiments performed on this sample (symbols). The figure also shows the fitting performed for all the experimental points (line). High repeatability was observed for the three measurements. All the points followed the same trend, and no systematic deviations were observed. The fitting was performed, and the equation obtained takes the following form:

$$V = a + b \times \Delta T \quad (1)$$

where ΔT is the temperature difference (in °C), and V represents the voltage (in mV). The adjusted coefficient of determination (Adj. R-square) for the linear equation was 0.9996, indicating that the linear equation could represent the test relationship between the voltage and temperature difference. Coefficients a and b are listed in a table as an inset in Figure 6(d). Based on the linear equation, the Seebeck coefficient of the ITO/AZO thin-film thermocouple had a constant value similar to the value of b (168 μV K^{-1}), which was twice as high as the Seebeck coefficient of 69 μV K^{-1} generated by the thin films, and about four times as high as that in previous work, [21] indicating that the interface donated the Seebeck coefficient of the thermocouple, while the ITO thin film acted as an electrode. Thus, approximately 99 μV K^{-1} was devoted to the connecting interface. A linear fitting was discarded because a large systematic deviation was observed above 500 ℃.

The total combined random error as a function of the temperature difference is shown in Figure 6(d). It shows error values lower than 1% for most of the measured temperature difference range (above 50 ℃), which is not surprising considering the

good repeatability of the three cycles measured. In conjunction with the large variation in the voltage with the temperature difference, the results prove the suitability and good reproducibility of the ITO/AZO thin-film thermocouples. The enhanced electrical properties of the thin-film thermocouple were attributed to the special defect structure of the AZO thin film.

4. Conclusions

Zinc-rich AZO columnar thin films were successfully prepared via sputtering deposition. The AZO films showed optimal growth along the direction of the (002) crystal plane, demonstrating a good crystallinity and high orientation, with few large-scale defects. However, many defects with a size of approximately 3–7 nm were formed by atom diffusion and point defect aggregation, leading to the destruction of the crystal structure and formation of a new structure. The Seebeck coefficient of the AZO thin film and interfacial electronic transport were the two contributors to the output voltage of the thin-film thermocouple, depending on the defect structure. On one hand, the cage defects were more stable than separate oxygen defects, leading to a stable Seebeck coefficient for the AZO thin film with increasing temperature. On the other hand, the interface voltage was generated by interfacial electron diffusion, which was affected by the carrier concentration and cage defects. Then, to fabricate a thermocouple, a zinc-rich AZO thin film was used as one of the two arms, with an ITO thin film with a band gap similar to that of the AZO thin film as the other arm. Furthermore, the Seebeck coefficient of the ITO/AZO thin-film thermocouple was constant at 168 $\mu V\ K^{-1}$. The thermocouple presented good repeatability after three

calibration cycles up to a hot-side temperature of 500 °C. The error values of the thin-film thermocouple were determined, and values lower than 1% were obtained for most of the measured temperature range. The zinc in the cage defects could be excited at high temperatures and capture electrons, leading to an increased difference in the carrier concentrations of the AZO and ITO thin films. Therefore, a thin-film thermocouple with a stable and enhanced electrical performance was obtained. These results showed that the construction of defect structures is a new and promising method to improve the stability of AZO-based thin-film thermocouples for high-temperature applications. Furthermore, the interfacial effect was generated by the connection between two kinds of N-type semiconductor, which could be used to bolster the performance of thermoelectric generators composed by two directly connected N-type or P-type materials.

Author contributions

The manuscript was written through contributions of all authors. All authors have given approval to the final version of the manuscript.

Conflicts of interest

There are no conflicts to declare.

Acknowledgements

The work was supported by the National Natural Science Foundation of China (Grant No. 61704006), the Scientific Research Project of Beijing Educational

Committee (Grant No. KM202111232015), Key Project of Independent Innovation Special Fund, AECC (Grant No. JK65200309), and the Spanish Agencia Estatal de Investigación under the Ramóny Cajal program (Grant No. RYC-2013-13970). Technical support of Raquel Oliver Valls and José Ortega Herreros is also acknowledged.

References

[1] S. H. Zaferani, M. W. Sams, R. Ghomashchi and Z. G. Chen, *Nano Energy*, 2021, **90**, 106572.

[2] Z. Guo, Y. Yu, W.Zhu, Q. Zhang, Y. Liu, J. Zhou, Y. Wang, J. Xing and Y. Deng, *Advanced Energy Materials*, 2022, **12**, 2102993.

[3] F. J. Disalvo, *Science*, 1999, **285**, 703.

[4] Y. Kashiwaya, C. E. Cicutti, A. W. Cramb and K. Ishii, *ISIJ International*, 1998, **38**, 348.

[5] D. Liu, P. Shi, W. Ren, Y. T. Liu, M. Liu, Y. J. Zhang, B. Tian, Q. J. Lin, Z. D. Jiang and Z. G. Ye, *Ceramics International*, 2018, **44**, S233.

[6] Y. T. Liu, W. Ren, P. Shi, D. Liu, Y. J. Zhang, M. Liu, Q. J. Lin, B. Tian and Z. D. Jiang, *Journal of Materials Science: Materials in Electronics*, 2019, **30**, 1786.

[7] Y. Liu, Y. Mitsutake and M. Monde, *International Journal of Heat and Mass Transfer*, 2020, **162**, 120331.

[8] M. Tougas Ian, A. Matin and J. Gregory Otto, *Sensors*, 2013, **13**, 15324.

[9] X. H. Zhao, Y. R. Wang, Y. Z. Chen, H. C. Jiang and W. L. Zhang, *Rare Metals*, 2017, **36**, 512.

[10] H. M. Tong, G. Arjavalingam, R. D. Haynes, G. N. Hyer and J. J. Ritsko, R*eview of Scientific Instruments*, 1987, **58**, 875.

[11] X. M. Chen, O. J. Gregory and M. Amani, *Journal of the American Ceramic Society*, 2011, **94**, 854.

[12] Y. T. Liu, W. Ren, P. Shi, D. Liu, Y. J. Zhang, M. Liu, Z. G. Ye, W. X. Jing, B. Tian and Z. D. Jiang, *Sensors*, 2018, **18**, 958.

[13] D. Liu, P. Shi, W. Ren, Y. T. Liu, G. Niu, M. Liu, N. Zhang, B. Tian, W. X. Jing, Z. D. Jiang and Z. G. Ye, *Journal of Materials Chemistry C*, 2018, **6**, 3206.

[14] W. H. Nam, Y. S. Lim, S. Choi, W. Seo and J. Y. Lee, *Journal of Materials Chemistry*, 2012, **22**, 14633.

[15] M. Zhang, Y. Tang, X. Tian, H. Wang, J. Wang and Q. Zhang, *Journal of Alloys and Compounds*, 2021, **880**, 160510.

[16] F. Xu and L. Sun, *Energy & Environmental Science*, 2011, **4**, 818.

[17] B. D. Boruah, *Nanoscale Advances*, 2019, **1**, 2059.

[18] D. Huang, W. L. Li, Z. F. Liu, Y. X. Li, C. Ton-That, J. Cheng, W. C. H. Choy and F. C. Ling, *Journal of Materials Chemistry A*, 2020, **8**, 4764.

[19] J. Nakamura, T. Fujitani, S. Kuld, S. Helveg, I. Chorkendorff and J. Sehested, *Science*, 2017, **357**, eaan8074.

[20] B. Zhou, L. Chen, C. Li, N. Qi, Z. Chen, X. Su and X. Tang, *ACS Applied*

Materials & Interfaces, 2020, **12**, 51669.

[21] H. Liu, X. Zhang, Q. Wang, Z. Liu, W. Chen, Q. Wang, H. Wang, W. Jiang, S. Liu, C. Liu, N. Wang, Y. Cui, Y. Ma and W. Ding, *Sensors and Actuators A Physical*, 2020, **311**, 112089.

[22] C. M. Pelicano and H. Yanagi, *Journal of Materials Chemistry C*, 2019, **7**, 4653.

[23] A. V. Kovalevsky, *Journal of Materials Chemistry A*, 2018, **6**, 13386.

[24] V. Karthikeyan, S. L. Oo, J. U. Surjadi, X. Li, V. C. S. Theja, V. Kannan, S. C. Lau, Y. Lu, K. Lam and V. A. L. Roy, *ACS Applied Materials & Interfaces*, 2021, **13**, 58701.

[25] A. Li, C. Hu, B. He, M. Yao, C. Fu, Y. Wang, X. Zhao, C. Felser and T. Zhu, *Nature Communications*, 2021, **12**, 5408.

[26] S. W. Feng, C. M. Lai, C. Y. Tsai, Y. R. Su and L. W. Tu, *Optical Materials Express*, 2013, **3**, 1777.

[27] S. Lim, H. Seok, M. Kwak, D. Choi, S. Kim, D. Kim and H. Kim, *Nano Energy*, 2021, **82**, 105703.

[28] G. J. Snyder, A. H. Snyder, M. Wood, R. Gurunathan, B. H. Snyder and C. Niu, *Adv. Mater.*, 2020, **32**, 2001537.

[29] Q. Sun, G. Li, T. Tian, Z. Man, L. Zheng, M. Barré, J. Dittmer, F. Goutenoire and A. H. Kassiba, *J. Eur. Ceram. Soc.,* 2020, **40**, 349.

[30] D. B. Zhang, H. Z. Li, B. P. Zhang, D. D. Liang and M. Xia, *RSC Advances* 2017, **7**, 10855.